

Collapse of the vortex-lattice inductance and shear modulus at the melting transition in untwinned $\text{YBa}_2\text{Cu}_3\text{O}_7$.

Peter Matl^{1,*}, N. P. Ong¹, R. Gagnon², and L. Taillefer^{2,†}

¹*Department of Physics, Princeton University, Princeton, New Jersey 08544* and

²*Department of Physics, McGill University, 3600 University Street, Montréal, Quebec, Canada H3A 2T8*

(Dated: November 11, 2018)

The complex resistivity $\hat{\rho}(\omega)$ of the vortex lattice in an untwinned crystal of 93-K $\text{YBa}_2\text{Cu}_3\text{O}_7$ has been measured at frequencies $\omega/2\pi$ from 100 kHz to 20 MHz in a 2-Tesla field $\mathbf{H} \parallel \mathbf{c}$, using a 4-probe RF transmission technique that enables continuous measurements versus ω and temperature T . As T is increased, the inductance $\mathcal{L}_s(\omega) = \text{Im } \hat{\rho}(\omega)/\omega$ increases steeply to a cusp at the melting temperature T_m , and then undergoes a steep collapse consistent with vanishing of the shear modulus c_{66} . We discuss in detail the separation of the vortex-lattice inductance from the ‘volume’ inductance, and other skin-depth effects. To analyze the spectra, we consider a weakly disordered lattice with a low pin density. Close fits are obtained to $\rho_1(\omega)$ over 2 decades in ω . Values of the pinning parameter κ and shear modulus c_{66} obtained show that c_{66} collapses by over 4 decades at T_m , whereas κ remains finite.

PACS numbers: 74.60.Ge, 74.72.Bk, 72.15.Gd, 64.70.Dv

I. INTRODUCTION

The investigation of the response of vortices in type II superconductors to an alternating driving current has had a long and fruitful history, beginning with the experiment of Gittleman and Rosenblum (GR) on PbIn and Nb alloys [1]. In cuprate superconductors, these investigations have been performed on $\text{YBa}_2\text{Cu}_3\text{O}_7$ (YBCO) over a broad range of frequencies extending from 100 kHz to a few THz. At frequencies ω below a few 100 MHz, the vortex response is obtained by directly measuring the sample’s complex resistivity $\hat{\rho}(\omega)$. At microwave frequencies (10 to 100 GHz), cavity perturbation techniques have been the primary approach, although bolometric absorption techniques have been more useful at the high microwave end.

The occurrence of the vortex solid-to-liquid melting transition in the cuprates is one of the most interesting phenomena in the investigation of ‘vortex matter’ in superconductors [2]. The melting transition at T_m has been investigated in some detail by high-resolution measurements of the magnetization [3, 4], heat capacity [5] and *dc* resistivity [6, 7]. In any solid-to-liquid transition, the key quantity of interest is the shear modulus which vanishes in the liquid. The resistivity profile (ρ vs. T) in a crystal of $\text{Bi}_2\text{Sr}_2\text{CaCu}_2\text{O}_8$ in which alternating strong and weak pinning channels are created by ion irradiation was interpreted as a loss of shear strength at T_m [8]. The effect of the vanishing shear modulus at T_m on ρ when the field \mathbf{H} is tilted relative to the twin boundaries in twinned YBCO crystals was also demonstrated [9].

The standard approach to investigating how the shear modulus changes in a system undergoing a solid-to-liquid transition is by observing its *dynamical response* to an oscillating driving force. The frequency dependence of $\hat{\rho}(\omega)$ in the vortex state in YBCO has been investigated by several groups at frequencies in the 1 to 100 MHz range. Initial measurements using thin-film samples found that

$\hat{\rho}(\omega) = \rho_1(\omega) + j\rho_2(\omega)$ displays strong, featureless dispersion at these frequencies [11, 12, 13]. However, the response in high-purity single crystals is qualitatively different. Wu, Ong, Gagnon and Taillefer (WOGT) [10] investigated the *ac* response in untwinned crystals of YBCO in the MHz range, and found that the inductance vs. H exhibits a step-wise change at the melting field. As a liquid cannot produce an inductive response, the step-wise change in the inductance is direct evidence for a collapse of the shear modulus c_{66} at T_m .

The 2-probe experiments of WOGT were performed at fixed T versus H . This approach cannot be extended to measurements in which T is continuously varied in fixed H because variations in the background signal (from T -dependent stray cable reactances) swamp the sample signal. We report results obtained by the use of an RF 4-probe technique that circumvents this obstacle. The 4-probe technique allows high-resolution impedance measurements versus each of the three quantities ω , H and T . We find that the collapse of the inductance is even more abrupt when T is scanned at fixed H . While we largely confirm the *fixed-T* results of WOGT, the *swept-T* experiments provide a more direct picture of the behavior of the vortex resistivity and inductance as T is increased above the melting line. With the broader perspective, we correct a previous inference regarding a ‘remanent’ shear modulus in the vortex liquid state. A detailed discussion of how the vortex-lattice inductance is separated from the ‘volume’ inductance is provided. Together with the measurements of WOGT, the present results provide a complete experimental picture of the linear response of the pinned lattice in a high-purity cuprate crystal to an *ac* driving current in the MHz frequency range. The two distinguishing features are the strong dispersion of $\hat{\rho}(\omega)$ observed even at low ω (just below the melting temperature T_m) and the striking abrupt collapse of the inductance at T_m .

To understand the spectra, we have adopted a model in

which the vortex lattice is weakly disordered by pinning to a low density of pins [16, 17]. A mean-field solution proposed by Ong and Wu (OW) [18] is used to fit the measured resistivity spectra. By measuring the damping viscosity $\eta(T)$ independently, we reduce the number of adjustable parameters to just 2 numbers at each T . We show that the OW solution can achieve close fits to $\rho_1(\omega)$ extending over 2 decades in ω . The fits enable us to find both κ and c_{66} (to within a multiplicative constant) at each T . The latter exhibits a remarkable 4-decade collapse to zero within 1 K of T_m .

In Sec. II a summary of the experimental approach is given. Section III discusses skin-depth effects and the ‘volume’ inductance. In Sec. IV, we report measurements versus T and H at constant ω . The central results – the spectra of ρ_1 and ρ_2/ω – are reported in Sec. V. Section VI explains the fits of the spectra to the weakly disordered lattice model, and Sec. VII discusses the temperature dependence of the shear modulus near T_m . Appendix A describes the 4-probe technique, while Appendix B summarizes the impedance calculation for a sample with elliptical cross-section. Appendix C summarizes the linear response of the weakly disordered lattice to an *ac* current.

II. EXPERIMENTAL DETAILS

As in WOGT [10], a weak, alternating current $\mathbf{J}e^{i\omega t}$ is applied within the CuO_2 plane ($\mathbf{J} \parallel \mathbf{a}$) in the presence of a field $\mathbf{H} \parallel \hat{\mathbf{c}}$. The average velocity response of the vortices is detected as a complex resistivity $\hat{\rho}(\omega) = \hat{v}(\omega)B/J_0$.

Because contact resistances on YBCO crystals are typically a fraction of an Ohm, they add a T -dependent background that dominates the sample signal. In an experiment in which the field H is swept at constant T (as in WOGT), this large background may be subtracted, by reference to the zero-field data at each T . However, when T is swept at constant H , the contact background leads to substantial errors. The problem is exacerbated by the T dependence of the dielectric filling in the long coax cables. We minimized this by using special cables with low-density Polytetrafluoroethylene (teflon) dielectric. The higher propagation velocity (0.85c versus 0.66c) is also an advantage.

The 4-probe design was developed to remove the background altogether. The sample (impedance $Z_s = R_s + j\omega L_s$) shunts the inner and outer conductors of both the incident and transmission coaxial cable (see Appendix A). If $Z_s \ll Z_0$ (the line impedance), the incident signal is strongly reflected, and the transmitted signal is highly sensitive to small changes in Z_s . By phase-detecting the latter we may determine Z_s . By inserting broad-band transformers in both the incident and transmission cables, we can achieve true 4-probe measurement at frequencies up to 50 MHz (Appendix A describes the calibration procedure).

The measurements were made on a detwinned crystal

of YBCO (of dimension $a = 1.11$ mm, $b = 0.41$ mm, and $c = 55$ μm), in which the *dc* resistivity displays a sharp transition (width of 0.2 K) at $T_c = 93.3$ K. The RF resistivity was measured with the RF current density $\mathbf{J} \parallel \mathbf{a}$, and $\mathbf{H} \parallel \mathbf{c}$. Although all measurements were performed in a screened room, radio broadcast signals are picked up as weak resonance lines in the spectra. Parasitic line resonances, detected as weak resonances, are the hardest to eliminate. However, they can be minimized by empirically adjusting the grounding strap configuration.

With the 4-probe method, we may vary independently each of the variables H (0-8 Tesla), ω (100 kHz to 20 MHz), and T . To confirm that we are in the linear-response regime, we checked that curves of $\hat{\rho}(\omega)$ measured with incident power at -15.5 dBm and at 4.5 dBm are closely similar (except for a higher noise content in the -15.5 dBm curve for ρ_2). We report all measurements in terms of the sample’s complex resistivity $\hat{\rho}(\omega) = Z_s(\omega)(bc/a') \equiv \rho_1(\omega) + j\rho_2(\omega)$, where $a' = 0.68$ mm is the separation of the voltage contacts. In place of $\rho_2(\omega)$, it is preferable to discuss the (specific) inductance defined by $\mathcal{L}_s \equiv \rho_2/\omega$ (note that $\mathcal{L}_s = L_s(bc/a')$). Dividing ρ_2 by ω isolates the divergent behavior of \mathcal{L}_s as $\omega \rightarrow 0$, thereby highlighting the dramatic collapse of \mathcal{L}_s at the lattice melting temperature.

III. SKIN-DEPTH AND VOLUME INDUCTANCE

In zero magnetic field, the impedance $Z_s(\omega)$ of a superconductor (in the form of a cylinder) may be calculated from the 2D Helmholtz equation $(\nabla^2 + \hat{\kappa}^2)\mathbf{A} = 0$, where $\hat{\kappa}^2 = \lambda^{-2} + 2j\delta^{-2}$ (here, λ is the London penetration length and δ the skin-depth determined by the quasiparticle conductivity).

First, we consider the normal-state impedance ($T > T_c$) by letting $\lambda \rightarrow \infty$, and replacing δ by the normal-state skin-depth $\delta_n = \sqrt{2\rho_n/\omega\mu_0}$ (where ρ_n is the normal-state resistivity and μ_0 the vacuum permeability). When ω is large enough that $\delta_n \ll \sqrt{A}$, J is confined to the skin-depth, and the effective $R_s(\omega)$ increases (A is the cross-section area). For a circular cross-section, $Z_s(\omega)$ is given by [20]

$$Z_s(\omega) = \frac{\omega\mu_0\ell\delta_n}{2\pi r_0\sqrt{2j}} \frac{J_0(\hat{x})}{J_1(\hat{x})}, \quad (1)$$

where $\hat{x} \equiv -jr_0\sqrt{2j}/\delta_n$, $J_m(\hat{x})$ is the Bessel function of order m , and r_0 (ℓ) is the radius (length) of the sample. The case of elliptical cross-section is treated in Appendix B.

Equation 1 shows that, at large ω , $R_s(\omega) \rightarrow \rho\ell/(2\pi r_0\delta_n)$, as expected. More important for our inductance discussion, the RF field energy at high ω is confined to the skin-depth. Therefore, the inductance $L_s(\omega)$ decreases monotonically to zero as $\omega \rightarrow \infty$. As this inductance expresses the RF energy stored in the volume

of a *straight* cylinder, we refer to it as the ‘volume’ inductance $L_{vol}(\omega)$ to distinguish it from the vortex-lattice inductance which is the main focus of this work (and from stray, geometric inductances that arise from coil-coil flux linkage). From Eq. 1, we find that

$$\lim_{\omega \rightarrow 0} L_{vol} = \frac{1}{2} \frac{\mu_0 \ell}{4\pi}. \quad (2)$$

For a high-purity Cu wire ($r_0 = 0.4$ mm, $\ell = 3$ mm) at 300 K, $L_{vol}(\omega)$ equals 120 pH at low ω , but falls to a tenth of this value at 20 MHz.

Below T_c , the penetration of the RF fields (in zero H) is set by the London length, i.e. $\hat{\kappa} \rightarrow \lambda^{-1}$. As the in-plane λ in YBCO is very short ($\sim 0.2\mu\text{m}$), we may regard the stored RF field energy to be nominally zero. Hence the change in L_s (in zero field) between T_c and, say 60 K, provides a direct measurement of L_{vol} . Applying Eq. 2 to a cylinder with circular cross-section area equal to that in our crystal, we find that $\lim_{\omega \rightarrow 0} L_{vol} = 34$ pH (corresponding to $\mathcal{L}_{vol} = 1.2 \times 10^{-13}$ Hcm). This tiny inductance may be measured with about 2% resolution by our 4-probe method.

In the resistive state ($H \gg H_{c1}$), the RF penetration is determined by $\rho_1(\omega)$ (i.e. $\hat{\kappa}^2 = 2j\delta_f^{-2}$, where the flux-flow skin-depth $\delta_f = \sqrt{2\rho_1/\omega\mu_0}$). As ρ_1 may be as large as $8\ \mu\Omega\text{cm}$ for $H = 2$ T, the volume inductance L_{vol} nearly recovers its full value given by Eq. 1. However, in our measurements, the inductance increase is actually far in excess of L_{vol} . The excess inductance arises purely from the vortex lattice.

Returning to the resistive component $R_s(\omega)$, we have converted it to ρ_1 by the assumption that \mathbf{J} is uniform over the cross-section (i.e. $\rho_1(\omega) = R_s(\omega)bc/a'$). However, if δ is comparable to the half-thickness $c/2$, $R_s(\omega)$ is significantly enhanced by the skin-depth effect, and ρ_1 will be overestimated. We now address this concern. As the aspect ratio $b/c \simeq 8.3$, we cannot rely on Eq. 1 for quantitative guidance. In Appendix B, we have calculated $Z_s(\omega)$ for a normal-state sample with an elliptical cross-section using Mathieu functions. The variation of $R_s(\omega)$ and $\mathcal{L}_{vol}(\omega)$ is shown in Fig. 1) for a sample with this high ellipticity. We assumed the normal-state resistivity $\rho_n = 4\mu\Omega\text{cm}$.

As the results depend only on δ_n , values for $R_s(\omega)$ and $L_{vol}(\omega)$ at other values of ρ_n are obtained by re-scaling the x -axis. For example, at 85.9 K, ρ_1 measured in a field of 2 T with $\omega/2\pi = 3$ MHz equals $\sim 1\mu\Omega\text{cm}$. Re-scaling the frequency axis in Fig. 1 by a factor of 4, we see that at $\omega/2\pi = 12$ MHz, $R_s(\omega)$ and $L_{vol}(\omega)$ deviate by only 5% and 3%, respectively, from their low-frequency (i.e. uniform-distribution) values. At the lowest T (< 84 K), however, the deviations may be up to 20% for $\omega/2\pi > 10$ MHz, but these low T -high- ω data will not play any significant role in our analysis. Throughout the low- ω region near the melting transition, the correction is less than 0.5 %, so that the uniform- J assumption is valid.

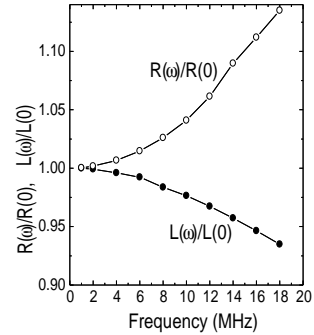


FIG. 1: Calculated impedance $Z_s(\omega) = R_s(\omega) + j\omega L_s(\omega)$ of a conducting cylinder of elliptical cross-section and resistivity $\rho = 4\mu\Omega\text{cm}$. The inductance L_s is entirely volume inductance L_{vol} . The parameters $\xi_0 \simeq 0.108$ and $h = 250\mu\text{m}$ are selected to match the sample cross-section.

IV. FIXED-FREQUENCY MEASUREMENTS

All the data reported here are taken either in zero field or in a fixed field of 2 T. In the resistive state, the inductance of YBCO varies strongly with ω and T . We first display the variation of $\mathcal{L}_s(\omega, T, H)$ versus T measured at selected ω in a 2-Tesla field as well as in zero field (main panel of Fig. 2). The inset shows the corresponding curves for ρ_1 .

In the main panel, we have plotted the specific inductance $\mathcal{L}_s = \rho_2/\omega$ with an arbitrary origin, because the total observed inductance L_{obs} is the sum of the sample contributions (L_{vol} and the vortex lattice term L_v) and an arbitrary background L_{bg} that arises from small uncertainties in setting ‘null’ in the phase setting of the lock-in amplifiers), viz.

$$L_{obs} = L_v + L_{vol} + L_{bg} \quad (3)$$

We take the portion of the curve at 1 MHz-0T below 90 K as our reference, and identify sample inductance signals relative to this reference curve.

We first discuss the 1 MHz curve in zero field. As T increases from 60 K, $\mathcal{L}_s(\omega_1, T, 0)$ is nearly T -independent until, at T_c , it undergoes a step-increase to the normal-state value ($\omega_1/2\pi = 1$ MHz). Clearly, the step corresponds to the collapse of the Meissner effect at T_c , as discussed above. The difference between $\mathcal{L}_s(\omega_1, T, 0)$ measured at 100 and 60 K gives $\mathcal{L}_{vol} = 1.0 \times 10^{-13}$ Hcm, rather close to the value 1.2×10^{-13} Hcm estimated below Eq. 2. Hence we identify the step change in the curve $\mathcal{L}_s(\omega_1, T, 0)$ with the maximum (specific) volume inductance \mathcal{L}_{vol} of our sample. The curve $\mathcal{L}_s(\omega_{15}, T, 0)$ measured at $\omega_{15}/2\pi = 15.4$ MHz shows a closely similar step, as expected from Meissner flux-expulsion.

When a field $H_0 = 2$ T is applied, the sample inductance is dominated by that of the vortex lattice. We follow the curve at 1 MHz and 2 T, starting at 60 K. As T increases, $\mathcal{L}_s(\omega_1, T, H_0)$ increases rapidly, rising to a cusp just below the melting temperature of the lattice

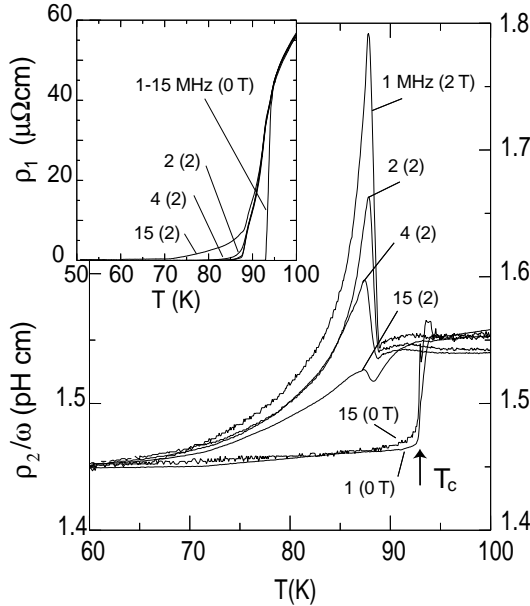


FIG. 2: (Main panel) Temperature dependence of the total sample inductance $\mathcal{L}_s(\omega, T, H) = \rho_2(\omega, T, H)/\omega$ measured in a 2-Tesla field ($\mathbf{H} \parallel \mathbf{c}$) at the frequencies indicated. Here, ‘15’ means 15.4 MHz and H (in Tesla) is in parentheses. As T approaches T_m from below, \mathcal{L}_s (measured at 1-4 MHz) rises to a sharp cusp before collapsing to the value \mathcal{L}_{vol} observed in the normal state. For comparison, the zero-field traces taken at 1 and 15.4 MHz are also shown. The inductance scale has an arbitrary origin (because of the term L_{bg} in Eq. 3). The portion of the curve 1 (0T) below 90 K serves as our reference line. Inductance signals measured relative to this reference are identified as contributions from the sample. The step-change at T_c in zero H reflects the Meissner expulsion of the stored RF field energy (reduction of volume inductance \mathcal{L}_{vol}). The inset shows ρ_1 measured at the same ω .

$T_m \simeq 88.5$ K. Curves at higher frequencies show a similar but reduced peak. Above T_m , \mathcal{L}_s collapses rapidly to a value very close to the normal state value. Because of the finite value of the RF vortex resistivity ρ_1 (inset), expulsion of the RF fields from the interior is now determined by the flux-flow skin-depth $\delta_f = \sqrt{2\rho_1/\mu_0\omega}$ ($\delta_f \gg \lambda$). At these temperatures, $\delta_f > c/2$, so the RF fields are uniform in the vortex liquid state; there is no change in \mathcal{L}_s in crossing $T_c = 93.5$ K.

The sharp increase in \mathcal{L}_s as T approaches T_m from below is one of our main results. The collapse of the inductance above T_m is the constant- H -scan version of the collapse observed by WOGT in constant- T scans versus H .

[As mentioned in Sec. I, the present swept- T scans provide a much clearer picture of how the inductance evolves into the normal-state value. In WOGT [12], the finite value of \mathcal{L}_s above the melting field H_m was interpreted as evidence for a small, residual shear rigidity in the vortex liquid state (their Fig. 1b). This inference is incorrect. As discussed here, the residual inductance above H_m is simply the volume inductance \mathcal{L}_{vol} . Within

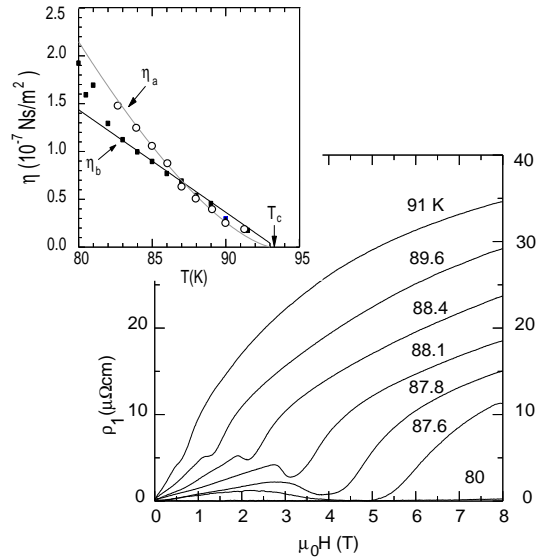


FIG. 3: The high frequency resistivity $\rho_1(\omega)$ measured at $\omega = 15.4$ MHz versus applied field $\mathbf{H} \parallel \hat{\mathbf{c}}$ at temperatures close to T_c in untwinned YBCO ($\mathbf{J} \parallel \hat{\mathbf{c}}$). The minimum is caused by the ‘peak effect’ which appears close to the melting field H_m . At each T , the initial slope of ρ_1 vs. H is used to determine the viscosity $\eta_a(T)$. The T dependence of η_a is plotted in the insert (η_b obtained from a second sample is also plotted). Near T_c , $\eta_a \sim (1 - T/T_c)^{1.5}$, while $\eta_b \sim (1 - T/T_c)$.

our resolution, the shear rigidity in the vortex liquid state is zero. This removes the need for the arbitrary ‘background’ liquid term ρ_2^b introduced by WOGT [10].]

At our highest frequencies, the lattice response is predominantly resistive. As discussed below, the friction term in this limit dominates the lattice forces and pinning forces, so that ρ_1 is proportional to the reciprocal of the viscosity $\eta(T)$. Figure 3 (main panel) displays the field dependence of $\rho_1(\omega)$ measured at the frequency $\omega/2\pi = 15.4$ MHz at temperatures close to T_c (the current is along the a -axis). At each T , we have fitted the initial slope to the (free) flux-flow expression $\rho_f = B\phi_0/\eta$ in order to find $\eta(T)$ (plotted in the insert) [$\phi_0 = h/2e$ is the flux quantum]. We measured $\eta(T)$ in 2 untwinned crystals. In the geometry $\mathbf{J} \parallel \mathbf{a}$, the uncertainty in determining η_a is large because the broad ‘peak effect’ restricts the range of H over which ρ_1 vs. H is truly linear. More reliable results are obtained (for η_b) in the geometry $\mathbf{J} \parallel \mathbf{b}$ where the peak effect is much narrower. The two sets of viscosity η_a and η_b are shown in Fig. 3 (insert). The viscosity data are used in the fits discussed in Sec. VI.

V. FREQUENCY DEPENDENCE OF THE COMPLEX RESISTIVITY

Figure 4 displays the frequency dependence of $\rho_1(\omega, T, H_0)$ at temperatures from 80.6 to 88.9 K (H is fixed at 2 T). At temperatures $T < T_m \sim 88.5$ K, the

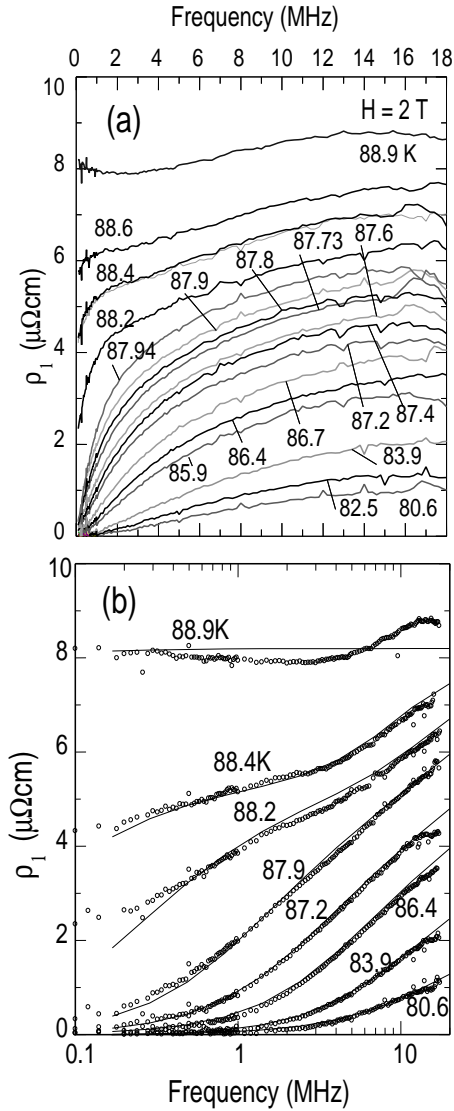


FIG. 4: (a) The frequency dependence of $\rho_1(\omega, T, H_0)$ at temperatures 80.6 to 88.9 K in a 2-Tesla field $\mathbf{H}_0 \parallel \mathbf{c}$. The curves for ρ_1 become increasingly ω dependent as $T_m(\sim 88.5 \text{ K})$ is approached from below. In the vortex liquid state above T_m , ρ_1 rapidly approaches a nominally ω -independent value (curve at 88.9 K). (b) A subset of the data in upper panel plotted against $\log \omega$ to show the low- ω region. The solid lines are fits discussed in Sec. VI.

value of ρ_1 in the limit $\omega \rightarrow 0$ is zero. However, above T_m , the limiting value becomes finite. At the highest ω , ρ_1 approaches the Bardeen-Stephen value for free flux-flow ρ_f (inset of Fig. 2).

Below T_m , ρ_1 is strongly dispersive. Close to T_m , ρ_1 displays a crossover from a sharply increasing region at low ω to a gradual region at high ω . The ‘knee’ feature separating the two regions rapidly moves to high frequencies as T falls below T_m by a few K, eventually moving out of our frequency window.

Figure 5 displays $\mathcal{L}_s(\omega, T, H_0)$ versus ω for temperatures below and above T_m (with $H_0 = 2 \text{ T}$). As explained

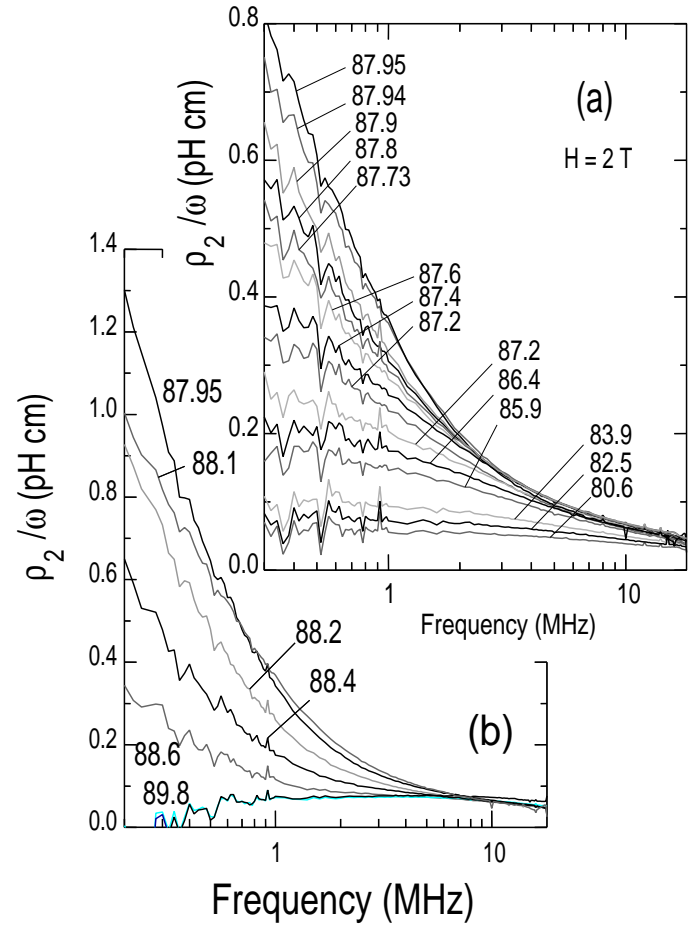


FIG. 5: The frequency dependence of the sample inductance $\mathcal{L}_s(\omega, T, H_0)$ measured in a 2-T field $\mathbf{H}_0 \parallel \mathbf{c}$. \mathcal{L}_s (referenced to the zero-field inductance curve) is the sum of \mathcal{L}_v and \mathcal{L}_{vol} . The upper and lower panels are measurements taken below and above 87.95 K, respectively. As $T \rightarrow T_m$ from below (a), the vortex term \mathcal{L}_v increases sharply, especially at low ω . Just below T_m (b), it collapses to zero, leaving the nominally flat spectrum that we identify as the volume inductance \mathcal{L}_{vol} .

following Eq. 3, we identify the sample inductance using the zero-field curve (below 90 K) as reference, viz.

$$\mathcal{L}_s(\omega, T, H) = [L_{obs}(\omega, T, H) - L_{obs}(\omega, T, 0)](bc/a')$$

As discussed in Sec. IV, \mathcal{L}_s rises to a sharp cusp as $T \rightarrow T_m^-$, before undergoing a steep collapse above T_m . The most pronounced dispersion occurs at low ω where \mathcal{L}_s shows divergent behavior in the limit $\omega \rightarrow 0$.

Although the spectra of the inductance are not used in our fitting process in Sec. VI, we discuss various contributions to the observed inductance signal (which includes the volume inductance) for the sake of completeness. We may estimate $\mathcal{L}_{vol}(\omega, T, H)$ by appealing to the observed ρ_1 and the calculated curves in Fig. 1. Note that \mathcal{L}_{vol} can never exceed 0.12 pHcm. At high frequencies, L_v is negligible, so that the curve at 15.4 MHz (2T) in Fig. 2 may be taken as that for \mathcal{L}_{vol} vs. T at large ω (we ignore

the slight dip near T_m). Using the values of ρ_1 measured at 15.4 MHz (Fig. 4), we find this interpretation is consistent with the calculations in Fig. 1.

We may also use the observed values of ρ_1 to estimate \mathcal{L}_{vol} at low frequencies. At the temperatures of interest (85-90 K), ρ_1 is sufficiently large, even at 200 KHz, to satisfy the uniform- J condition, i.e. \mathcal{L}_{vol} is close to its maximum value 0.12 pHcm. With increasing ω , \mathcal{L}_{vol} decreases slowly to its high- ω value as seen in Fig. 2. For example, at 88.2 K (in Fig. 5b), our estimate of the volume inductance spectrum is a curve that starts at 0.12 pHcm at low ω and decreases slowly to ~ 0.06 pHcm at high ω . The divergent vortex term is easy to distinguish from this small, featureless background.

This concludes the purely experimental part of the report. The spectra in Figs. 4 and 5, complemented by the measurements of WOTG [10], constitute a rather complete quantitative description of the linear-response of the vortex lattice in untwinned YBCO at RF frequencies. In the following sections, we interpret the measurements within a specific model, in order to extract the temperature dependence of the vortex-lattice shear modulus.

VI. FITS TO THE SPECTRA

A. Discussion of the model

In the model used by GR [1], the vortex equation of motion is

$$\eta \ddot{\mathbf{u}} + \kappa \mathbf{u} = \mathbf{J} \times \hat{\mathbf{z}}\phi_0, \quad (4)$$

where \mathbf{u} is the vortex displacement from equilibrium, and η and κ are the damping viscosity and the Labusch parameter, respectively, and $\mathbf{B} \parallel \hat{\mathbf{z}}$. Measurements of $\hat{\rho}$ in thin-film samples [11, 12] and in untwinned crystals [10] of YBCO are in strong disagreement with the Lorentzian response $\hat{\rho} = (B\phi_0/\eta)[1 - j\omega_p/\omega]^{-1}$ predicted by Eq. 4 (here $\omega_p \equiv \kappa/\eta$). In particular, the dramatic dispersion observed when the lattice melting line is approached, in either constant- H scans (WOGT) or in the constant- T scans reported here, cannot be reproduced by Eq. 4, even if one replaces κ by an ‘effective’ parameter that depends on ω and B .

In the context of the vortex glass [14], Dorsey [15] has derived scaling relations for the ω -dependent conductivity $\hat{\sigma}(\omega)$ at the vortex glass-to-liquid transition, viz. $\hat{\sigma}(\omega) \sim (-i\omega)^\alpha$. In *thin-film* samples of YBCO, the measured spectra do in fact display power laws in ω over 2-3 decades (1-500 MHz) [12]. The situation in untwinned crystals is very different, however. The spectra reported here (and in WOGT [10]) do not follow power laws at all. Further, the melting transition is abrupt and weakly first-order rather than the continuous transition of the vortex glass. Under the high-purity conditions found in untwinned YBCO crystals, the observed spectra are more consistent with that of a weakly disordered vortex lattice with random pins than a vortex glass (as we now show).

In their theory of the depinned vortex lattice, Schmid and Hauger [16] and Larkin and Ovchinnikov [17] represented the rigidity of the moving periodic structure by the lattice force matrix $\mathbf{D}_{l,m}^s$. As discussed below, the non-Debye spectrum of $\hat{\rho}(\omega)$ and its rapid change vs. T in the vicinity of T_m reflect a rapidly changing length-scale in the problem. To describe this, it is necessary to retain the \mathbf{q} (wavevector) dependence of the Fourier transform $D_s(\mathbf{q})$ of $\mathbf{D}_{l,m}^s$. (Clem and Coffey [19] have shown that approximating $D_s(\mathbf{q})$ by a constant D merely reproduces a Debye-like spectrum.) With inclusion of the pinning forces, the equation of motion is [16]

$$\eta \ddot{\mathbf{u}}_i + \sum_{i'} \mathbf{D}_{l,i'} \cdot \mathbf{u}_{i'} + \kappa \sum_i \mathbf{u}_i \delta_{l,i} = \mathbf{J} \times \hat{\mathbf{z}}\phi_0, \quad (5)$$

where the sites with pins are indexed by i (the pinning force is short-ranged). To match the strong dispersion observed, OW assumed that the pin distribution is sparse [18] ($R_0 \gg a_B$, where R_0 is the average pin separation, and $a_B = \sqrt{\phi_0/B}$ the lattice spacing). Appendix C summarizes the solution of OW.

In response to the driving current $\mathbf{J}e^{j\omega t}$, the magnitude and phase of the vortex velocity (averaged over the sample) produces the ac voltage that determines $\hat{\rho}$. At low ω , the inter-vortex forces dominate the friction force $\eta \dot{\mathbf{u}}$, so the velocity response is predominantly inductive ($\omega \mathcal{L}_v \gg \rho_1$). In the opposite limit of large ω , $\eta \dot{\mathbf{u}}$ is dominant. As $\mathcal{L}_v \rightarrow 0$, ρ_1 approaches the free-flow value $B\phi_0/\eta$. Thus \mathcal{L}_v is a measure of the average restraining force on each vortex. It is largest if the restraining forces are dominant, but vanishes when viscous damping dominates.

The main feature of the solution is that the lattice propagator $G(\mathbf{R}, \omega)$, which transmits information on the vortex displacement at site \mathbf{R} to its surroundings, has an *effective range* $R_G = a_B \sqrt{c_{66}/\eta\omega}$ that varies as $1/\sqrt{\omega}$ (Eq. 26). At low frequencies, $R_G \gg a_B$, which implies that the motion of any one vortex is strongly correlated with that of a huge number of neighbors, a subset of which are pinned (the 2D correlation volume is $\sim R_G^2$). Hence the velocity response is large and inductive. With increasing ω , the average vortex is restrained by fewer and fewer pinned vortices as R_G shrinks. The in-phase (dissipative) component of the average velocity increases, while the inductance drops. When ω exceeds the characteristic frequency

$$\omega_{66} = \frac{4\pi c_{66}}{\eta} \frac{a_B^2}{R_0^2}, \quad (6)$$

R_G falls below the average pin spacing R_0 . The majority of vortices now respond as if they are free, and ρ_1 rapidly approaches the Bardeen-Stephen free flux-flow value $\rho_f = B\phi_0/\eta$ while \mathcal{L}_v decreases to zero.

The crossover is observed as the knee in ρ_1 at T just below T_m (see Fig. 4a). As T approaches T_m from below, the rapid softening of c_{66} causes this crossover to occur at progressively lower frequencies. Finally, in the liquid

state above T_m , the vanishing of c_{66} implies that virtually all the vortices are decoupled from the pins: ρ_1 equals ρ_f at all ω in the RF range, while \mathcal{L}_v is zero.

B. The fitting procedure

As discussed in Appendix C, the OW solution has 4 adjustable parameters at each T , viz. $\kappa(T)$, $c_{66}(T)$, $\eta(T)$ and R_0 . Empirically, the fits are not sensitive to the particular choice of R_0 (as long as $R_0 \gg a_B$). Following WOGT, we set $R_0 = 7 a_B$ for $B = 1$ T.

As discussed in Sec. IV, the viscosity $\eta(T)$ may be obtained from the initial slope of ρ_1 vs. H measured at 15.4 MHz (Fig. 3). Adopting the viscosity data in the insert of Fig. 3, we then have only *two* adjustable parameters at each T , viz. $\kappa(T)$ and $c_{66}(T)$ [equivalently, $\omega_p(T)$ and $\omega_{66}(T)$]. As we have a *continuous* spectrum measured over 2 decades in frequency to find 2 numbers, the fitting problem is evidently strongly over-constrained.

The fitting procedure consists in selecting seed values for ω_p and ω_{66} so that the quantity $\hat{\mathcal{S}}(\omega)$ (Eq. 22) can be computed by summing the propagator $G_{2D}(\mathbf{R}_i, \omega)$ (Eq. 28) over an area much larger than R_G^2 (the pins are arrayed in a triangular superlattice of spacing R_0 , and the sum is typically extended to 12 impurity ‘shells’ from the origin). With $\hat{\mathcal{S}}(\omega)$, we may compute the complex resistivity $\hat{\rho}(\omega)$, viz.

$$\hat{\rho}(\omega) = \left(\frac{B\phi_0}{\eta} \right) \left[1 - \left(\frac{\omega_p a^2}{j\omega R_0^2} \right) \frac{1}{1 + \hat{\mathcal{S}}(\omega)} \right]. \quad (7)$$

The calculated curve is then compared with the measured spectra of $\rho_1(\omega)$, and the fit parameters are changed in an iterative manner until the fit is optimized (the inductance data are not used in the optimization). For spectra near T_m , the high-frequency curvature is most sensitive to ω_p whereas the curvature at low ω is largely determined by the choice of ω_{66} , as expected on physical grounds (the value of η mainly fixes the overall scale of ρ_1). As shown in Fig. 4b, close fits to the data are achieved over the 2-decade range of ω . At low ω , the calculated ρ_1 is capable of matching the curvature of the measurements to a surprising degree (with only 2 adjustable parameters). The close agreement achieved in Fig. 4b offers encouraging support for the validity of the model.

C. Calculated inductance

With the parameters ω_p and ω_{66} optimized at each T , we may calculate the vortex-lattice inductance \mathcal{L}_v . As discussed above, in the limit $\omega \rightarrow 0$, the extended range of the propagator $G_{2D}(R, \omega)$ implies that each vortex is restrained by a great many pins. Hence the velocity response is purely inductive. The calculated \mathcal{L}_v displays the strong divergence observed in the RF measurements.

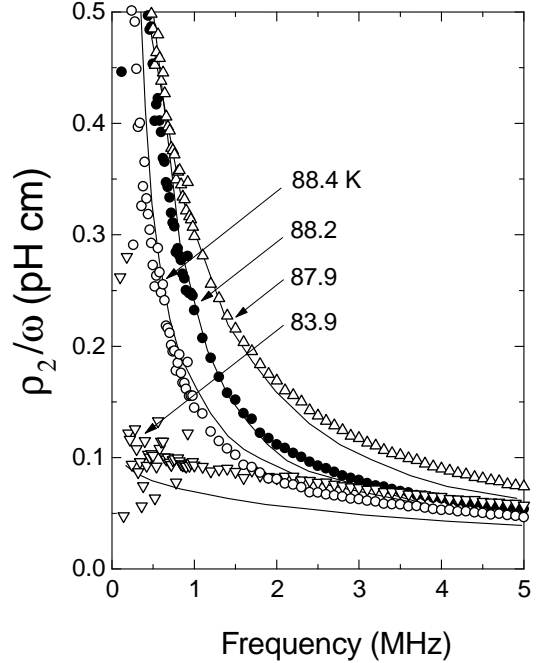


FIG. 6: Comparison of calculated $\rho_2(\omega)/\omega$ (solid lines) with the measured vortex inductance $\mathcal{L}_v(\omega, T, H_0)$ (open symbols) over the frequency range 100 kHz to 20 MHz in a field $H_0 = 2$ T. $\rho_2(\omega)/\omega$ is calculated from Eq. 7 using the values of ω_p and ω_{66} derived from the fits to ρ_1 in Fig. 4b. The estimated volume inductance has been subtracted from the total sample inductance (see text). Above 87 K, \mathcal{L}_v strongly diverges as $\omega \rightarrow 0$, while at 83.9 K, the divergence is not observed.

In Fig. 6, we compare at 4 selected T the calculated \mathcal{L}_v (solid lines) with the observed \mathcal{L}_v (open symbols).

The sample inductance is the sum of the vortex-lattice term \mathcal{L}_v and the volume inductance \mathcal{L}_{vol} , viz.

$$\mathcal{L}_s(\omega, T, H) = \mathcal{L}_v(\omega, T, H) + \mathcal{L}_{vol}(\omega, T, H). \quad (8)$$

The volume term cannot be measured directly at low ω because it is much weaker than the vortex term. However, at frequencies above ~ 3 -10 MHz (depending on T), it accounts for nearly all of the sample inductance (see Sec. IV). Because of this uncertainty, we used the spectra of ρ_1 to optimize the fit parameters.

The contribution of the volume inductance has to be estimated to isolate the vortex-lattice term (Eq. 8). In Sec. IV, this was carried out using the observed ρ_1 together with calculations for a sample with elliptical section. The estimated \mathcal{L}_{vol} has been subtracted to isolate the vortex term \mathcal{L}_v in the plots displayed in Fig. 6. Although the uncertainties in the estimated \mathcal{L}_{vol} are largest at low ω , they have the least impact on the comparison because \mathcal{L}_s diverges steeply in this limit. The comparison (inset) shows good agreement between calculation and measurement above 87 K (no further refinements of the fit parameters were made in comparing with \mathcal{L}_v). As T approaches $T_m \simeq 88.5$ K, the low- ω divergence in the observed \mathcal{L}_v progresses to lower frequencies (see the

curves at 87.9, 88.2 and 88.4 K in inset). The calculated curves also match this progression. At low T , however (83.9 K curve), the agreement is not as good because the uniform- J assumption used to extract $\hat{\rho}$ is increasingly suspect.

VII. FIT RESULTS

A. Collapse of the shear modulus

The values of $\kappa(T)$ and $c_{66}(T)$, obtained from $\omega_p(T)$ and $\omega_{66}(T)$, respectively, are shown in panels (a) and (b) of Fig. 7. In each case, we show two sets of values depending on whether η_a or η_b has been used in the fits. We interpret the decrease of κ as $T \rightarrow T_c$ (Panel (a)) as reflecting the decrease in condensation energy. We note that κ remains finite at the melting temperature T_m . Hence our fit strongly argues against models in which the transition at T_m is interpreted in terms of a vanishing κ .

The critical parameter is the shear modulus c_{66} which undergoes a steep collapse by more than 3 decades within an interval of 1 K. The collapse occurs over the background (gradual) decrease of c_{66} associated with the power-law decrease of the condensate density as $T \rightarrow T_c$. Because of the rapid collapse in c_{66} , the steep increase in \mathcal{L}_s at temperatures below T_m is interrupted. Within a 1-K interval, \mathcal{L}_s drops to its normal-state value (background curve in Fig. 7b).

Each of the discrete data points for c_{66} is derived from a full spectrum for ρ_1 . To follow the collapse in more detail, we have also adopted a different procedure, using the 1 MHz curve for \mathcal{L}_s and ρ_1 measured *continuously* vs. T , together with interpolated values of η_a and η_b . This allows us to determine c_{66} as a continuous curve very close to T_m (the fitting procedure becomes unstable at lower T). We show these continuous curves as solid and broken lines in Fig. 7b. At low T , the continuous-fit values are slightly larger than the spectra-based fits which are more accurate, but close to T_m , they match very well. The continuous curve allows us to monitor the decrease of c_{66} over 4 decades.

From Fig. 7, we conclude that the transition at T_m is associated with a rapid collapse of the shear modulus. However, the Labusch parameter κ remains finite. This provides firm evidence that the transition involves the *collapse of the shear modulus*, rather than the vanishing of the Labusch parameter.

B. Summary

In summary, we have performed measurements of $\hat{\rho}(\omega)$ of the vortex lattice in an untwinned YBCO crystal to investigate the collapse of the lattice inductance at the melting temperature, using a high-resolution 4-probe RF technique. At all T investigated, the resistivity $\rho_1(\omega)$ is strongly dispersive. Over the frequency range 100

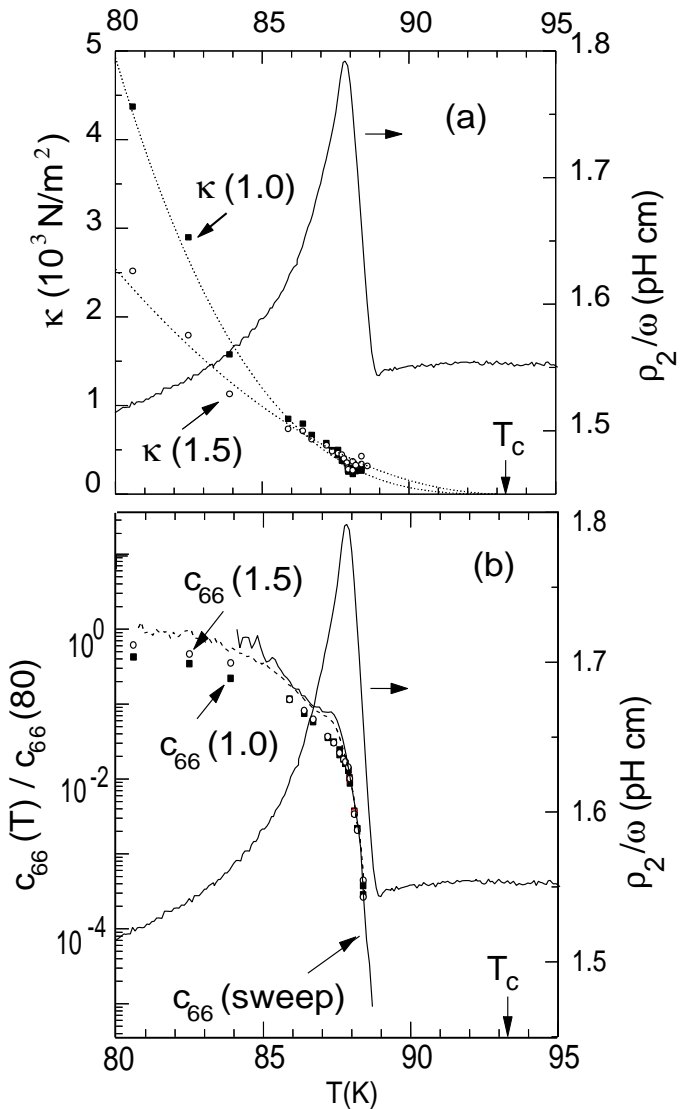


FIG. 7: (a) Values of the Labusch parameter κ obtained from the fits, using either η_a (open circles) or η_b (solid squares). The sharp peak (right scale) is the behavior of the sample inductance $\mathcal{L}_s = \rho_2/\omega$ measured at 1 MHz in a 2-T field [the zero of \mathcal{L}_s is arbitrary (Sec. IV)]. (b) The normalized shear modulus c_{66} (log scale) versus T obtained from the fits, using either η_a (open circles) or η_b (solid squares) in Fig. 3. Near T_m , c_{66} decreases by 4 orders of magnitude within an interval of 0.5 K. The solid line represent values of c_{66} obtained from fits to $\hat{\rho}(\omega)$ with ω fixed at 1 MHz, and $H=2$ T, using η_b . The dashed line is obtained with ω fixed at 2 MHz, but using η_a .

kHz - 20 MHz, ρ_1 increases from zero to the free-flow value $B\phi_0/\eta$, with a cross-over frequency scale (ω_{66}) that rapidly decreases towards zero as T approaches the melting temperature T_m from below. In the solid phase, the inductance ρ_2/ω displays a steep divergence as $\omega \rightarrow 0$. However, at T_m , this low-frequency divergence collapses to give an ω -independent inductance in the vortex-liquid state above T_m . The observed spectra are qualitatively different from those in thin-film YBCO, and incompati-

ble with the predictions of vortex glass theory. To extract the vortex-lattice shear modulus from these spectra, we have used the mean-field solution of the Schmid-Hauger-Larkin-Ovchinnikov model to fit the complex resistivity spectra. From the 2-parameter fit at each temperature, the normalized shear modulus $c_{66}(T)$ displays a remarkable 4-decade collapse towards zero at T_m . Hence the observed collapse of the inductance is driven by the vanishing of the shear modulus rather than the vanishing of the pinning strength κ .

Appendix A: Experimental details

We describe first the 2-probe method used by WOGT [10]. The sample Z_2 bridges the inner and outer conductors of both the incident and transmission coax cables of line impedance Z_0 (Fig. 8a). The load resistors Z_1 and Z'_1 are 100Ω thin-film resistors. This configuration maximizes the sensitivity of the transmitted wave to small changes in Z_2 when $|Z_2| \ll Z_0$. The incident wave is transmitted with transmission coefficient Γ_T , and reflected with reflection coefficient Γ_R , where

$$\Gamma_T = \frac{2Z_0Z_2}{Z_2(2Z_0 + Z_1 + Z'_1) + (Z_0 + Z_1)(Z_0 + Z'_1)}, \quad (9)$$

$$\Gamma_R = \Gamma_T \frac{Z_0 + Z'_1}{Z_0 + Z_1} + \frac{Z_1 - Z_0}{Z_1 + Z_0}. \quad (10)$$

Phase-sensitive detection of the transmitted signal allows Z_2 to be determined (Fig. 8a). The incident power from a synthesizer (Hewlett Packard 3336C) is typically fixed at $+4.5$ dBm, corresponding to a current less than 5 mA at the sample. The transmitted signal is phase-detected by a high-frequency lock-in Extender/Enhancer (Palo Alto Research PAR100), which down-converts signals in the range 1-25 MHz to 1-50 kHz, suitable for a standard lock-in amplifier (Stanford Research SR830).

To modify the technique for 4-probe measurements (Fig. 8a), we inserted an RF transformer T1 of bandwidth 10 kHz - 150 MHz (Mini-Circuits T1-6-KK81) at the output of the synthesizer. The transmitted signal passes through a second transformer T2 before entering the PAR100. In Fig. 8b, the contact impedances are represented by the impedances Z_{si} and Z'_{si} . The transmission and reflection coefficients are now

$$\Gamma_T = \frac{2\xi_2}{(1 + \xi_T)(1 + \xi'_T) - \xi_2^2}, \quad (11)$$

$$\Gamma_R = \frac{(\xi_T - 1)(1 + \xi'_T) - \xi_2^2}{(1 + \xi_T)(1 + \xi'_T) - \xi_2^2}, \quad (12)$$

where $\xi_T = (Z_1 + Z_{s1} + Z_2 + Z_{s3})/Z_0$, $\xi'_T = (Z'_1 + Z'_{s1} + Z_2 + Z'_{s3})/Z_0$, and $\xi_2 = Z_2/Z_0$.

While the 4-probe method provides much higher resolution, a drawback is that the inserted transformers introduce strong reflections. The largest reflection comes from the upstream transformer T1. A wave reflected from the

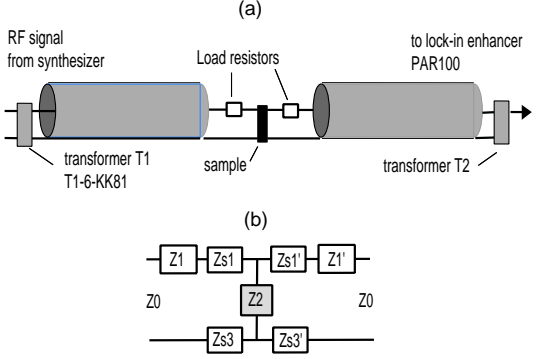


FIG. 8: (a) Schematic diagram of the measurement circuit. The sample shunts the inner and outer conductors, so that the transmitted signal is highly sensitive to slight changes in the sample impedance Z_2 . Transformers T1 and T2 are inserted to decouple grounds in the 4-probe technique. The lower figure (b) shows the labelling of the contact impedances Z_{si} , Z'_{si} , which may greatly exceed Z_2 in amplitude.

sample is reflected again at T1 and adds an ω -dependent contribution to the original transmitted wave.

The effect of the multiply reflected wave on the total transmitted signal at the detector is expressed as

$$\Gamma_T^{obs} \equiv \frac{V_{out}}{V_{in}} = e^{j k \ell_{tot}} \Gamma_T \Gamma_T^1 [1 + e^{j 2 k \ell_1} \Gamma_R \Gamma_R^1 + \dots], \quad (13)$$

where Γ_T^1 and Γ_R^1 are, respectively, the transmission and reflection coefficients of T1. The path-lengths from T1 to the detector, and from T1 to the sample, are called ℓ_{tot} and ℓ_1 , respectively. Higher-order reflection contributions (notably from T2) are indicated by \dots . In addition, we are now also sensitive to slight ω -dependent deviations from unity of the PAR100's transfer function $\hat{g}(\omega)$.

To compensate for these two background contributions, we used a reference combination $Z_r, Z_{1,r}, Z'_{1,r}$ tailored to have a reflection coefficient Γ_R^r nearly equal to that of the sample (hereafter, Γ_R^s). As $|Z_s| \ll 1$, the sample's Γ_R^s is very close to 0.33, with Z_1 and $Z'_1 = 100\Omega$. The best choice for the reference combination is $Z_r = 10\Omega$, and $Z_{1,r} = Z'_{1,r} = 90.9\Omega$, which has an ω -independent Γ_R^r of 0.3344, and a transmission coefficient $\Gamma_T^r = 0.044$.

With the sample in place, the signal presented at the input of the SR 830 lock-in is given by $V_s = \hat{g}(\omega) V_{out}(Z_s)$, where V_{out} is given by Eq. 13. If the sample (and load resistors) are replaced by the reference combination, we have $V_r = \hat{g}(\omega) V_{out}(Z_r)$. Dividing these two equations removes $\hat{g}(\omega)$. This leaves the multiple reflection factor (quantity in $[\dots]$ in Eq. 13). However, as Γ_R^s and Γ_R^r are nearly identical by design, the leading term in $[\dots]$ is the same (the other terms are down by a factor $\Gamma_T^r \ll 1$). Hence we have

$$\frac{V_s}{V_r} = \frac{\Gamma_T^s}{\Gamma_T^r} [1 + \mathcal{O}(\Gamma_T^s)], \quad (14)$$

where Γ_T^s and Γ_T^r are given by Eq. 11 with $Z_2 = Z_s$ and Z_r , respectively. Our procedure is to measure and store the curve of V_r vs. ω at each temperature of interest. Then V_s is measured versus ω . Since Γ_T^r is known, Γ_T^s (and Z_s) may be calculated from V_s and V_r using Eq. 14. We checked the reliability of the procedure using a second reference consisting of just a single 50- Ω resistor connecting the inner conductors of the two coax cables (this also has $\Gamma_R^r = 0.333$, but a much larger $\Gamma_T^r = 0.667$).

Appendix B: Impedance of a conductor with elliptical cross-section

The impedance $Z_s(\omega)$ of a conductor with elliptical cross-section is obtained by solving the 2D Helmholtz equation $(\nabla^2 + \kappa^2)\mathbf{A} = 0$ in elliptical coordinates (ξ, η) , where $\kappa^2 = 2j\delta_n^{-2}$. With $\mathbf{A}(\xi, \eta) = \psi(\xi)\phi(\eta)\hat{\mathbf{z}}$, the Helmholtz equation separates into the two Mathieu equations, viz. [21]

$$\frac{d^2\psi}{d\xi^2} - [a(\hat{q}) - 2\hat{q}\cosh 2\xi]\psi = 0, \quad (15)$$

$$\frac{d^2\phi}{d\eta^2} + [a(\hat{q}) - 2\hat{q}\cos 2\eta]\phi = 0, \quad (16)$$

where $\hat{q} \equiv -\kappa^2 h^2/4$ (h is the foci spacing). With the boundary condition $A(\xi_0, \eta) = A_S$ (i.e. a constant on the surface S), the vector potential may be expanded in terms of the Mathieu functions as

$$A(\xi, \eta) = \sum_{n=0}^{\infty} c_{2n} Ce_{2n}(\xi, \hat{q}) ce_{2n}(\eta, \hat{q}). \quad (17)$$

Ce_{2n} is expressed by the expansion $Ce_{2n}(\xi, \hat{q}) = \sum_{r=0}^{\infty} A_{2r}^{(2n)} \cosh(2r\xi)$ [the same expansion holds for ce_{2n} , but with $\cos(2r\eta)$ in place of $\cosh(2r\xi)$].

The Mathieu functions are not tabulated because the separation parameter $a(\hat{q})$ and the coefficients $A_{2r}^{(2n)}$ are functions of \hat{q} . For a given \hat{q} , $a(\hat{q})$ satisfies the continued fraction $a = -(\hat{q}^2/2)/[1 - (a/4) - (\hat{q}^2/64)/[1 - \dots]]$ [21]. We truncated the continued fraction at the 12th order. The 12 roots $\{a_n(\hat{q})\}$ generate the full matrix $A_{2r}^{(2n)}$ with $(n, r) = 1, \dots, 12$.

Finally, with the ac voltage $V(\omega) = -j\omega A_S$ and the ac current $I = -\hat{\kappa}^2/\mu_0 \int_S d\xi d\eta A(\xi, \eta)$, the impedance may be expressed as

$$Z_s(\omega) = \frac{j\omega\ell\mu_0}{(2\pi)^2} \left[\sum_n \frac{(A_0^{(2n)})^2}{\mathcal{L}_{2n}} \frac{Ce'_{2n}(\xi_0, \hat{q})}{Ce_{2n}(\xi_0, \hat{q})} \right]^{-1}, \quad (18)$$

where $Ce'_{2n} = \partial Ce_{2n}/\partial\xi$, and $\mathcal{L}_{2n} = \int_0^{2\pi} ce_{2n}^2(\eta, \hat{q}) d\eta$. In Fig. 1, we display the ω dependence of $R_s(\omega)$ and $\mathcal{L}(\omega)$ calculated with parameters $\xi_0 \simeq 0.108$ and $h = 250\mu\text{m}$, matching the sample cross-section, and $\rho_1 = 4\mu\Omega\text{cm}$.

Appendix C: The solution of Ong and Wu

We summarize the equations in Ref. [18]. The displacement \mathbf{u}_i of a vortex at site i is described by the equation

$$\eta\ddot{\mathbf{u}}_i + \sum_{s,m} \mathbf{D}_{i,m}^s \cdot \mathbf{u}_m + \kappa \sum_{pins i} \mathbf{u}_i \delta_{i,i} = \mathbf{J} \times \hat{\mathbf{z}}\phi_0. \quad (19)$$

Only a subset of vortices (at sites indexed by i) are affected by the pins. The remaining vortices are ‘free’, apart from being restrained by the lattice forces represented by $\mathbf{D}_{i,m}^s$ ($s = T, L$ indexes the polarization mode). The displacement at an arbitrary site i is related to the displacement of the pinned vortices by

$$\begin{aligned} \mathbf{u}_i(\omega) = & \left(\frac{J\phi_0}{j\omega\eta} \right) \hat{\mathbf{y}} - \frac{\kappa}{N} \sum_{pins i} \mathbf{u}_i(\omega) \cdot \\ & \times \sum_{s,q} \frac{\hat{\mathbf{e}}_s(\mathbf{q}) \hat{\mathbf{e}}_s(\mathbf{q}) e^{j\mathbf{q} \cdot (\mathbf{R}_i - \mathbf{R}_i)}}{[D_s(\mathbf{q}) + j\omega\eta]}, \end{aligned} \quad (20)$$

where $\hat{\mathbf{e}}_s(\mathbf{q})$ is the unit vector for the mode s .

At the mean-field level, the displacement of the vortex at a pin-site \mathbf{u}_{imp} is

$$\mathbf{u}_{imp}(\omega) = \hat{\mathbf{y}} \left(\frac{J\phi_0}{j\omega\eta} \right) \frac{1}{1 + \hat{\mathcal{S}}(\omega)}, \quad (21)$$

where all the interaction effects are in the term

$$\hat{\mathcal{S}}(\omega) \equiv \frac{\omega_p a^2}{j\omega R_0^2} + \kappa[G(0, \omega) + \sum'_i G(\mathbf{R}_i, \omega)], \quad (22)$$

and $\omega_p \equiv \kappa/\eta$ is the pinning frequency. The lattice propagator $G(\mathbf{R}, \omega)$ is defined as [16, 18]

$$G(\mathbf{R}, \omega) = \frac{1}{N} \sum_{sq} \frac{(\hat{\mathbf{y}} \cdot \hat{\mathbf{e}}_s(\mathbf{q}))^2 e^{j\mathbf{q} \cdot \mathbf{R}}}{[D_s(\mathbf{q}) + j\omega\eta]}. \quad (23)$$

In Eq. 22, the first term represents the uniform $\mathbf{q}=0$ mode of the transmitted elastic forces. The remaining terms are elastic forces transmitted to the pinned vortex at the origin $\mathbf{0}$ arising from its own displacement ($G(0, \omega)$), or the displacement of other pinned vortices $\sum'_i G(\mathbf{R}_i, \omega)$ (the prime indicates that the $i = \mathbf{0}$ term is left out).

Neglecting the longitudinal modes, the transverse force matrix is expressed as [16]

$$D_T(\mathbf{q}) = [c_{66}q^2 + c_{44}q_z^2]a_B^2. \quad (24)$$

where q is the in-plane component of \mathbf{q} , viz. $\mathbf{q} = (q, q_z)$, and c_{66} and c_{44} are the shear and tilt moduli, respectively.

In the 2D limit, the propagator simplifies to the form (after angular-averaging within the ab plane and neglecting the tilt modulus c_{44})

$$\kappa G_{2D}(\mathbf{R}_\perp, \omega) = g \int_0^Q dq \frac{q J_0(qR)}{[q^2 + jp^2]}. \quad (25)$$

where $Q = \sqrt{4\pi/a_B^2}$, $J_0(x)$ is the zeroth order Bessel function, $R = |\mathbf{R}_\perp|$, with $\mathbf{R} = (\mathbf{R}_\perp, R_z)$, and g the coupling constant $\kappa/4\pi c_{66}$. The frequency dependence appears only in the characteristic wavevector

$$p = \sqrt{\frac{\eta\omega}{c_{66}a_B^2}} \quad (26)$$

which serves as a cut-off of the logarithmic divergence in the 2D case. Setting $R = 0$ in Eq. 25, we have

$$\kappa G_{2D}(0, \omega) = g \left[\ln \sqrt{\left(1 + \frac{Q^4}{p^4}\right)} - j \arctan\left(\frac{Q^2}{p^2}\right) \right]. \quad (27)$$

As the propagator $G_{2D}(R, \omega)$ is used repeatedly in the sum in Eq. 22, it is convenient to adopt the approximation (accurate to a few percent)

$$\kappa G_{2D}^a(R, \omega) = g \left\{ \ln \sqrt{\left[\frac{(\gamma R)^4 + p^{-4}}{(\gamma R)^4 + Q^{-4}} \right]} - j \arctan\left(\frac{Q^2}{p^2}\right) \frac{1}{[1 + (\beta p R)^2]^2} \right\}, \quad (28)$$

with $\beta = 0.52$ and $\gamma = 0.85$. Equations 27 and 28 were given incorrectly in OW [18] (*cpf* their Eqs. 18 and 19).

Acknowledgments

We thank Hui Wu for generous assistance and helpful advice. N.P.O. acknowledges support from the U.S. Office of Naval Research (Contract N00014-01-0281) and the New Energy and Industrial Tech. Develop. Org. (NEDO), Japan. R.G. and L.T. are funded by NSERC of Canada and FCAR of Quebec. L. T. acknowledges support from the Canadian Inst. for Advanced Research and the A.P. Sloan Foundation.

*Present address of P.M.: Koch Industries, 20 East Greenway Plaza, Houston, TX 77046.

†Present address of L. T.: Department of Physics, University of Toronto, Toronto, Ontario, CANADA M5S 1A7.

[1] J.I. Gittleman and B. Rosenblum, Phys. Rev. Lett. **16**, 734 (1966).
[2] For a review, see G. Blatter, M. V. Feigel'man, V. B. Geshkenbein, A. I. Larkin, and V. M. Vinokur, Rev. Mod. Phys. **66**, 1125 (1994).
[3] E. Zeldov, D. Majer, M. Konczykowski, V. B. Geshkenbein, V. M. Vinokur, and H. Shtrikman, Nature **375**, 373 (1995).
[4] U. Welp, J. A. Fendrich, W. K. Kwok, G. W. Crabtree, and B. W. Veal Phys. Rev. Lett. **76**, 4809 (1996).
[5] A. Schilling, R. A. Fisher, N. E. Phillips, U. Welp, D. Dasgupta, W. K. Kwok, and G. W. Crabtree, Nature **382**, 791 (1996).
[6] W. K. Kwok, S. Fleshler, U. Welp, V. M. Vinokur, J. Downey, G. W. Crabtree, and M. M. Miller, Phys. Rev. Lett. **69**, 3370 (1992); W. K. Kwok *et al.*, Phys. Rev. Lett. **72**, 1088 (1994).
[7] H. Safar, P. L. Gammel, D. A. Huse, D. J. Bishop, J. P. Rice, and D. M. Ginsberg, Phys. Rev. Lett. **69**, 824 (1992).
[8] H. Pastoriza and P. H. Kes, Phys. Rev. Lett. **75**, 3525 (1995).
[9] W. K. Kwok, J. A. Fendrich, V. M. Vinokur, A. E. Koshelev, and G. W. Crabtree, Phys. Rev. Lett. **76**, 4596 (1996).
[10] Hui Wu, N. P. Ong, R. Gagnon and L. Taillefer, Phys. Rev. Lett. **78**, 334 (1997).
[11] H. K. Olsson, R.H. Koch, W. Eidelloth, and R. P. Rober-tazzi, Phys. Rev. Lett. **66**, 2661 (1991).
[12] Hui Wu, N. P. Ong and Y. Q. Li, Phys. Rev. Lett. **71**, 2642 (1993).
[13] Dong H Wu, J. C. Booth and Steven M. Anlage, Phys. Rev. Lett. **75**, 525 (1995).
[14] D. S. Fisher, M. P. A. Fisher, and D. A. Huse, Phys. Rev. B **43**, 130 (1991).
[15] Alan T. Dorsey, Phys. Rev. B **43**, 7575 (1991).
[16] Albert Schmid and Wolfgang Hauger, Jnl. Low Temp. Phys. **11**, 667 (1973).
[17] A. I. Larkin and Yu. N. Ovchinnikov, Zh. Eksp. Teor. Fiz. **65**, 1704 (1973) [Sov. Phys. JETP **38**, 854 (1974)].
[18] N.P. Ong and Hui Wu, Phys. Rev. B **56** 458 (1997).
[19] J. R. Clem and Mark W. Coffey, Phys. Rev. B **46**, 14662 (1992).
[20] See for e.g., *Classical Electromagnetic Radiation*, 3rd ed., M. A. Heald and J. B. Marion (Saunders College Pub. N.Y., 1995), p. 190.
[21] N. W. McLachlan, *Theory and applications of Mathieu functions* (Oxford, 1947), Chs. III and XVII.